

www.acsanm.org Article

Visualizing the Effect of Oxidation on Magnetic Domain Behavior of Nanoscale Fe₃GeTe₂ for Applications in Spintronics

Yue Li, Xiaobing Hu, Arash Fereidouni, Rabindra Basnet, Krishna Pandey, Jianguo Wen, Yuzi Liu, Hong Zheng, Hugh O. H. Churchill, Jin Hu, Amanda K. Petford-Long, and Charudatta Phatak*

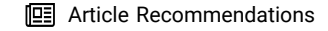


Cite This: ACS Appl. Nano Mater. 2023, 6, 4390-4397



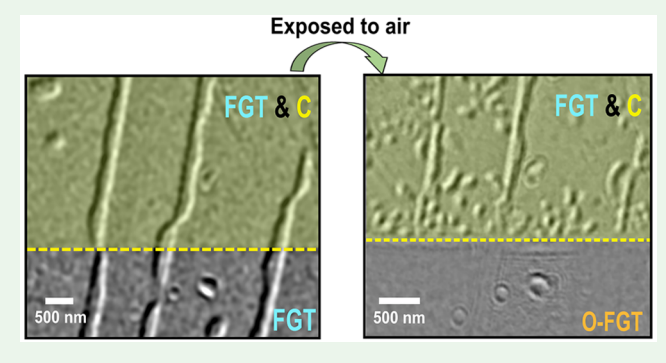
ACCESS I

III Metrics & More



s Supporting Information

ABSTRACT: Magnetic van der Waals (vdW) materials offer an opportunity to design heterostructures that will lead to exotic functionalities that arise from interfacial interaction. In addition to coupling to different vdW materials, the naturally oxidized surface layer of a vdW material also forms a heterostructure with its bulk film, giving rise to intriguing phenomena. Here, we directly observe the impact of oxidation on the magnetic domains, namely, magnetic stripe domain and skyrmions, in a nanoscale Fe₃GeTe₂ flake using cryo Lorentz transmission electron microscopy. After the Fe₃GeTe₂ is exposed to ambient conditions, partial oxidation leads to an increase in the density of skyrmions even under zero magnetic field. Complete oxidation leads to a loss of the magnetic



domain structure. We observe a gradual change in Fe_3GeTe_2 from single crystal to amorphous as the oxidation increases. The oxidized Fe_3GeTe_2 primarily consists of iron oxide, which could be antiferromagnetic in nature. We hypothesize that the interfacial interaction between these surface antiferromagnetic oxides and the bulk ferromagnetic Fe_3GeTe_2 , as well as the effect of interfacial roughness, leads to the increase in Néel skyrmion creation. This work opens a path to harness controlled oxidation as a build block to create dense skyrmion lattices without the need for an external magnetic field, leading to potential future applications in spintronic devices.

KEYWORDS: Fe₃GeTe₂ oxidation, LTEM, Neel skyrmions, rich—Fe-Ge cluster, interfacial interaction

1. INTRODUCTION

Two dimensional (2D) magnetic van der Waals (vdW) materials, that consist of a stack of atomic layers, exhibit weak interlayer vdW interactions and strong intralayer interactions. This unique structure and strong anisotropy, in addition to the different compositions and stackings that can arise, gives rise to rich emergent physical behaviors, for example, low-dimension-limit ferromagnetism, a broad range of magnetic spin textures,³⁻⁶ and a Curie temperature that can be tuned by external stimuli such as thickness, strain, and ion irradiation. 7-9 VdW heterostructure stacks containing magnetic vdW materials can be easily engineered using mechanicalassembly and stacking, both by using the exfoliation method or by interfacing with thin films deposited using various sample growth methods. The flexibility of the heterostructures that can be created enables a variety of novel functionalities that result from interfacial coupling, 10,11 for example, exchange bias, 12,13 and magnetic proximity effects. 14 This class of materials is therefore attracting broad interest due not only to enabling an understanding of fundamental physical phenomena but also to their potential as candidates for spintronic^{15,16} and valleytronic¹⁷ applications.

Fe₃GeTe₂ (FGT) has been extensively explored to understand its intrinsic magnetic,² electronic,⁷ and optical¹⁸ behaviors. In addition, the effect of interfacial interactions has been explored by creating heterostructures with different materials, e.g., WTe₂,³ CrI₃,¹⁹ and MnPS₃.²⁰ FGT is known to be unstable under ambient conditions,^{12,21,22} with easy formation of a surface oxidized FGT (O-FGT) layer. Interestingly, the formation of O-FGT naturally creates an interface with bulk FGT resulting in emergent physical phenomena, e.g., exchange bias,¹² antiferromagnetic coupling,²¹ and an interfacial Dzyaloshinskii—Moriya interaction (DMI).²² Unlike the above-mentioned heterostructures by externally stacking different materials, the O-FGT layer will have strong interaction with the bulk FGT. Although complete oxidation of transition metals can degrade their magnetic properties, partially oxidized magnetic films can exhibit

Received: December 21, 2022 Accepted: March 1, 2023 Published: March 10, 2023





anomalous magnetic phenomena, such as an additional unidirectional anisotropy seen in Co/CoO and Fe/Fe $_2$ O $_3$. Thus, understanding the impact of oxidation on magnetic properties of vdW magnets especially in terms of domain behavior is critical for future applications, such as bioinspired computing and infomration storage. However, so far, the impact of oxidation on magnetic domain is little known.

In this work, we explore how the oxidation affects the magnetic behavior of nanoscale FGT flake. The nanoscale-size magnetic domains are directly image in the FGT prior to and post oxidation, by the use of Lorentz transmission electron microscopy (LTEM). Comparisons of the structure and composition of the FGT and the O-FGT enable us to understand the phase changes introduced by oxidation, using high-resolution transmission electron microscopy (HRTEM) and energy-dispersive X-ray spectroscopy (EDS), respectively. The oxidation state in the O-FGT is further analyzed by means of electron energy loss spectroscopy (EELS) to gain insight into the nature of the Fe valence in the FGT oxides. Our findings demonstrate that the oxidation to a certain extend in the FGT boosts the creation of skyrmions due to the interfacial interaction between antiferromagnetic O-FGT and ferromagnetic FGT.

2. EXPERIMENTAL SECTION

2.1. FGT Crystal Growth. FGT single crystals were grown by a chemical vapor transport method using I_2 as a transport agent. The mixture of Fe, Ge, and Te powders with stoichiometric ratio was sealed in a evacuated quartz tube and heated under a temperature gradient from 700 to 600 $^{\circ}$ C in a two-zone tube furnace. Millimetersize single crystals were obtained for 1 week's growth. The composition and structure of the obtained crystals were checked by EDS and X-ray diffraction, respectively.

2.2. Preparation of TEM specimen. Bulk FGT crystals were exfoliated inside a nitrogen glovebox (H_2O , $O_2 < 0.5$ ppm) . A 27 nm thick flake, which are measured using atomic force microscopy (AFM) (Supporting Information Figure S1), was selected^{2.5} and transferred onto a 50 nm thick SiN_x membrane TEM window using a dry transfer method involving polydimethylsiloxane (PDMS) and polycarbonate (PC). The residual PC was removed by thermally annealing at 350 °C and a vacuum of 2e - 2 mbar for 3 h, in a vacuum chamber connected to the glovebox. An approximately 5 nm thick graphite flake was then transferred to cover part of the FGT flake using a similar method, to protect the covered area from oxidization.

The cross-section TEM specimens for HRTEM, EDS, and EELS were also prepared from the bulk FGT crystal using a Zeiss focused ion beam (FIB) system. To prepare the TEM sample for HRTEM experiment, a carbon layer was deposited a using E-beam in the FIB to protect the surface O-FGT layer from FIB damaging. The lamella was further thinned from around 200 nm thick to less than 30 nm by low-energy Ar ions using a Gatan PIPS II system to prepare a damage-free sample. For a EELS TEM sample, a 110 nm thick Au layer was deposited on the surface using DC sputtering to protect the surface O-FGT during FIB preparation. The thickness of this FIB lamella is approximately 65 nm that was estimated by the means of SEM. More details on the TEM samples can be found in the Supporting Information Figure S1.

2.3. LTEM Measurement. The LTEM imaging was performed using a FEI Tecnai F20ST TEM operating in Lorentz mode at 200 kV. A Gatan double-tilt liquid nitrogen holder, with a minimum reachable temperature of 100 K, was utilized to carried out cryo LTEM experiments. Both fresh FGT and O-FGT flakes were imaged using a zero-field-cooling protocol from room temperature to 100 K. The defocus used for the LTEM images was 8–10 mm.

2.4. TEM Experiments. HRTEM imaging of the FGT samples was performed using a JEOL JEM-2100F TEM operating at 200 kV,

as well as a chromatic-aberration-corrected FEI Titan TEM operating at 200 kV. The EDS data were collected using an FEI Talos F200X STEM equipped with a super-X quad detector. The EELS data were collected using a JEOL ARM200CF aberration-corrected STEM equipped with a Gatan Quantum Dual EELS system, operating at 200 kV. The background signal was removed using the power-law fitting method. The position of the Fe- $L_{2,3}$ edge was determined by fitting the spectrum using a Gaussian function. The white line ratio of L_3/L_2 was calculated using the Pearson method with a double step function. The calibration samples for the EELS measurements were an Fe (99.95%) film, a sample taken from a Fe₂O₃ crystal, and Fe₃O₄ nanopowder (MilliporeSigma).

3. RESULTS

3.1. Observation of the Effect of Oxidation on Magnetic Domain Structure. The FGT sample was cooled in the absence of magnetic field from room temperature to 100 K. Figure 1a shows an LTEM image of the pristine FGT flake:

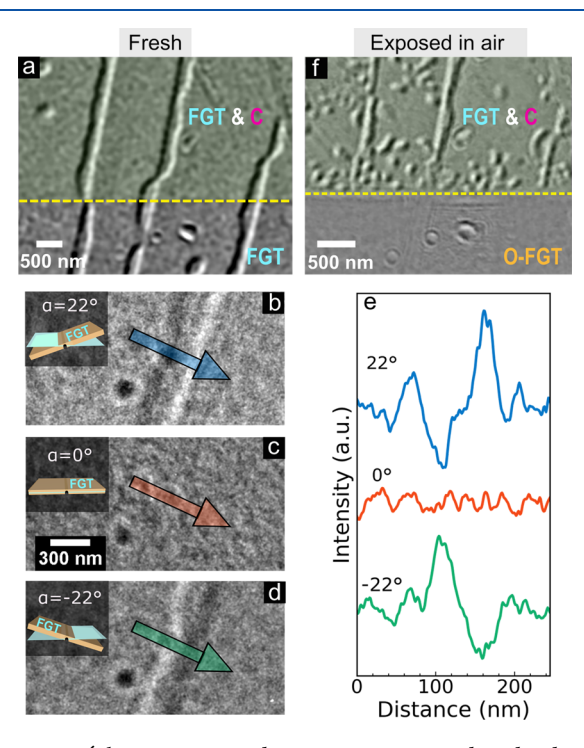


Figure 1. Néel-type magnetic domains in pristine and oxidized FGT. (a) Background-subtracted LTEM image showing magnetic domains of pristine FGT flake in a zero-field cooled at 100 K, where the yellow dashed line indicates the boundary of the graphite capping layer and 'FGT & C' represents the sample region with the FGT sample and the top graphite layer. LTEM images of Néel-type stripe domain as a function of sample tilt: (b) $\alpha = 22^\circ$, (c) $\alpha = 0^\circ$ and $\alpha = -22^\circ$. Inset: schematic illustrates the FGT sample tilt direction. (e) Average intensity line profiles across the stripe domains shown by colored arrows in (b–d). (f) Magnetic stripe domains and Néel skyrmions in the same FGT flake after exposure to air for a week.

magnetic stripe domains and a few magnetic skyrmions being visible at 100 K. These domains and skyrmions were confirmed to be Néel-type by acquiring a tilt series of out-of-focus LTEM images as shown in Figure 1b—d. Figure 1e shows that dark-bright (bright-dark) intensity profile at $\alpha=22^\circ$ ($\alpha=-22^\circ$) and a flat line at $\alpha=0^\circ$, confirming that the contrast disappears at zero-tilt conditions. This suggests that the observed magnetic domains are of Néel-type in the fresh FGT with strong magnetic perpendicular anistropy. Note that the

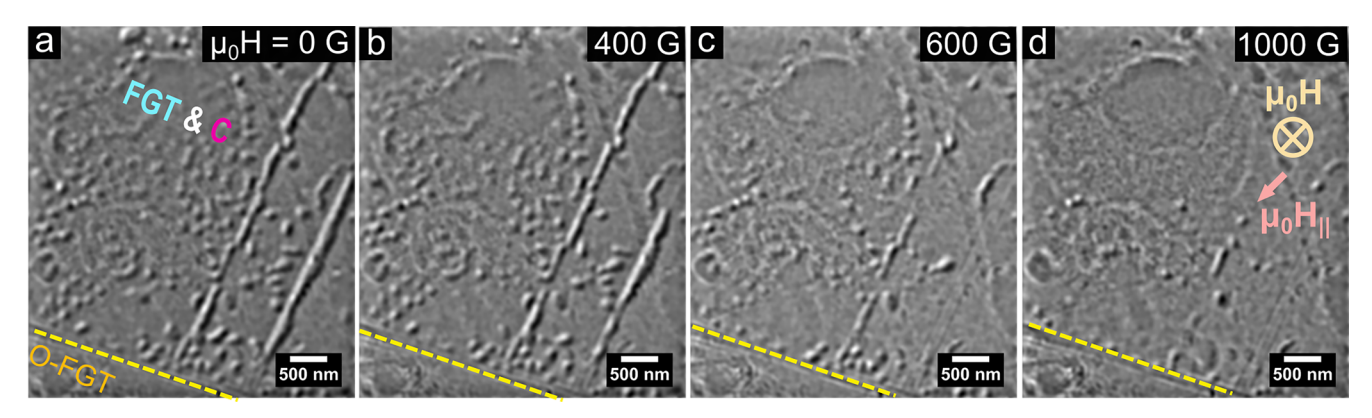


Figure 2. (a–d) Response of magnetic domains to the strength of a perpendicular magnetic field (μ_0H) (sample tilt angle $\alpha=23^\circ$). An in-plane magnetic field component, μ_0H_{\parallel} , is also introduced due to the sample tilt. The yellow dashed line indicates the boundary of the graphite capping layer. Magnetic contrast was obtained by subtracting the image acquired at different magnetic field strengths from the image recorded at 1500 Oe, at which the magnetic domains are saturated. The 'FGT & C' in (a) indicates the region with the FGT sample and the protective graphite layer.

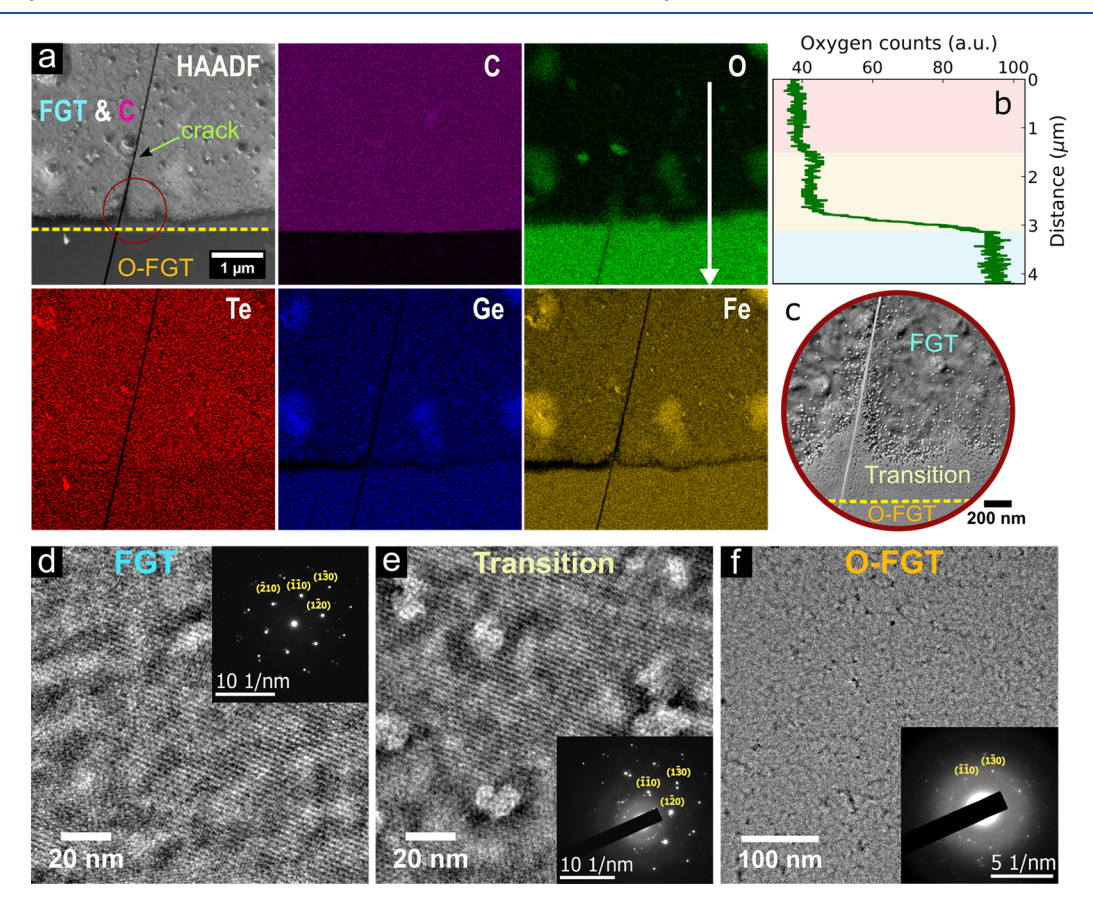


Figure 3. Analyses of composition and crystal structure of an FGT flake on a SiN_x membrane. (a) HAADF-STEM image and elemental maps. The zone axis of the flake is along [001]. (b) Oxygen content across the region marked by a white arrow in the O EDS map in (a). (c) Bright-field TEM image showing FGT, a transition region close to the grapite cap boundary, and the O-FGT. HRTEM images of (d) pristine FGT and (e) transition region, and (f) TEM image of the O-FGT region with selected-area diffraction pattern inset.

image shown in Figure 1a was obtained by subtracting two LTEM images at α tilt angles of -22° and 22° , respectively. This was done to improve the magnetic contrast as the raw LTEM images (Supporting Information Figure S2) show very weak magnetic contrast due to small flake thickness. At opposite tilt angles, the orientations of the in-plane magnetization components, which are perpendicular to the electron beam, are opposite to one another. This allows for separating the contribution from the magnetic phase shift in the LTEM images. In Figure 1a, two of the magnetic stripe domains run

continuously across the boundary between regions that are covered by the graphite capping layer and uncovered (see Supporting Information Figure S1), indicating that the entire FGT flake is in the as-prepared state and is not oxidized.

It is well-established that FGT forms a surface oxide layer under ambient conditions. ^{12,21,22,30} Thus, in order to investigate how the FGT oxidation affects the behavior of magnetic domains, the identical FGT specimen was exposed to air for a week, so that an O-FGT surface layer formed on the region that is not protected by graphite. Figure 1f shows an

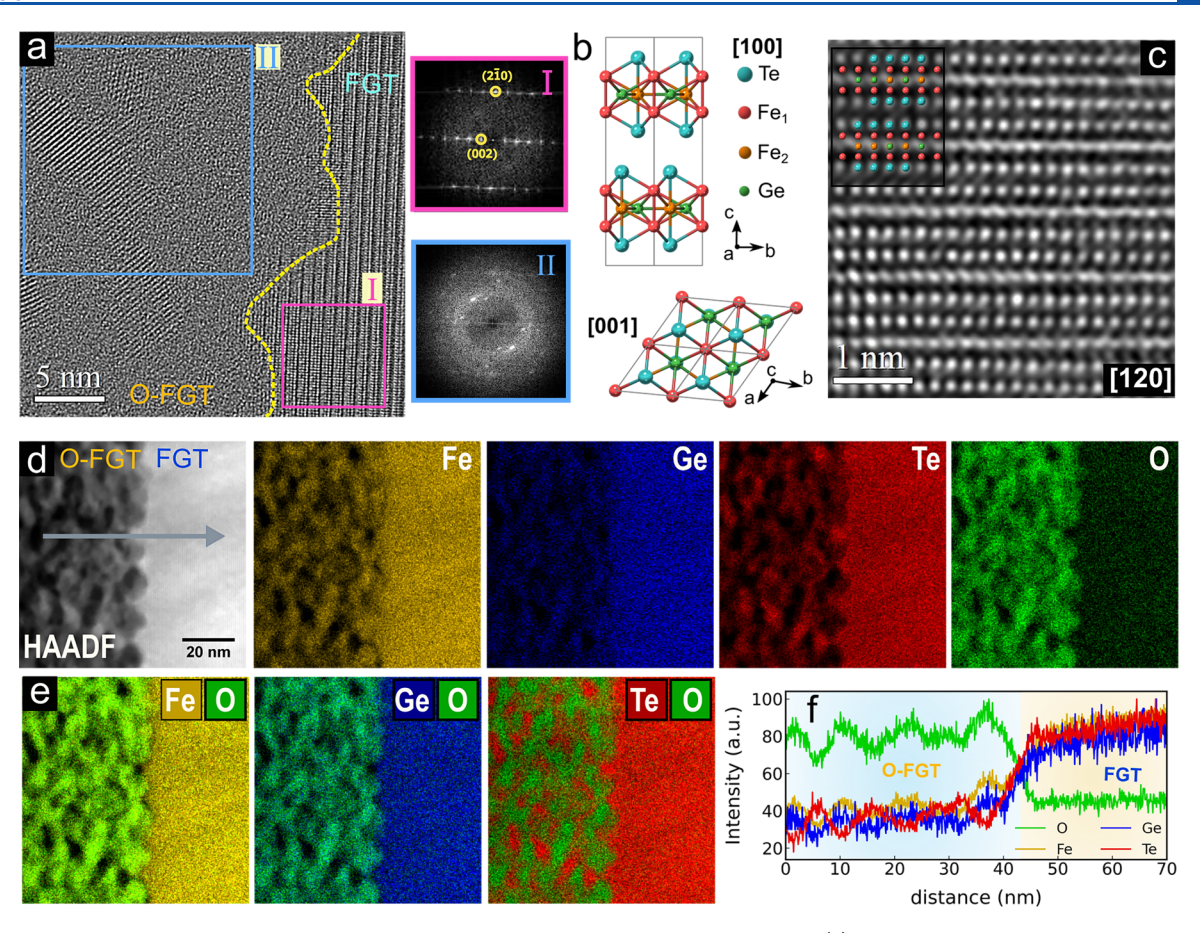


Figure 4. Crystal structure and elemental composition in a cross-section specimen of bulk FGT. (a) HRTEM image showing the crystal structure of FGT and O-FGT: yellow dashed line indicates the interface. Insets: FFT patterns of Regions I and II marked by colored frames in (a). (b) Schematics of the FGT crystal structure along the [100] and [001] zone axes. (c) Atomic-resolution TEM image of the bulk FGT along the [120] zone axis, which matches the standard atomic structure (inset). (d) HAADF-STEM image and STEM EDS composition maps for Fe, Ge, Te, and O. (e) Superposition of O STEM EDS map with those of Fe, Ge, and Te. (e) Average line profiles of O, Fe, Ge, and Te across the O-FGT and FGT regions indicated by a gray arrow in the STEM-HAADF TEM image in (d).

image of the same region of the flake as imaged in Figure 1a, after exposure to air. The O-FGT region shows no magnetic contrast owing to sample degradation arising from oxidation. Surprisingly, in the region of FGT covered by graphite, densely packed Néel skyrmions are formed, especially close to the edge of the graphite. The magnetic contrast in the FGT flake after exposure to air was further affected by artifacts caused by oxidation of the sample. Therefore, in order to discern the magnetic contrast and observe it clearly, we also separated out the magnetic phase shift contribution, using the abovementioned image subtraction approach.

Additionally, we also explored the response of magnetic domains to externally magnetic field in the O-FGT. Increase in the applied magnetic field strength leads to shrinking and annihilation of magnetic domains, in which the magnetization original orientation is antialigned with the direction of the applied magnetic field that is polarized with increasing field (Figure 2). This further confirms that the extracted magnetic contrast originates from the magnetic phase. A 1500 G externally magnetic field is needed to polarize the magnetization in the imaging region, which is greater than the saturation field (1000 G) required for a 60 nm thick FGT flake.³¹ To understand the underlying mechanism of how oxidation affects the FGT and promotes the formation of Néel skyrmions in a zero-field condition, we explored the elemental composition and crystal structure in FGT and O-FGT.

3.2. Chemical and Structural Characterizations. We characterized the spatial distribution of composition in the FGT flake after exposure to air using scanning TEM (STEM) EDS analysis. The high-angle annular dark field (HAADF) STEM image and composition maps seen in Figure 3a shows that overall the elements are spatially homogeneous except for a few regions that are richer in Fe, Ge, and O in the FGT covered by the graphite cap. This may result from the penetration of oxygen during air exposure. The relative distribution of O is also shown as a line scan in Figure 3b along the white arrow indicated in the O elemental map of Figure 3a. The fully exposed area of FGT (referred to here as O-FGT) has the highest O concentration, and it gradually decreases to a very low concentration as we move toward the graphite-covered region. There is a slightly higher O content near the graphite boundary. The bright-field TEM image shown in Figure 3c shows the presence of a transition region between the O-FGT and the pristine FGT. The brighter particles observed in this region and along the crack in the graphite layer correspond to the oxidized FGT. By correlating the compositional distribution to the observed magnetic domain behavior, we can conclude that the fully oxidized FGT suppresses the formation of magnetic domains or skyrmions, while a small amount of oxygen promotes the creation of dense Néel skyrmions in the FGT. Oxygen atoms

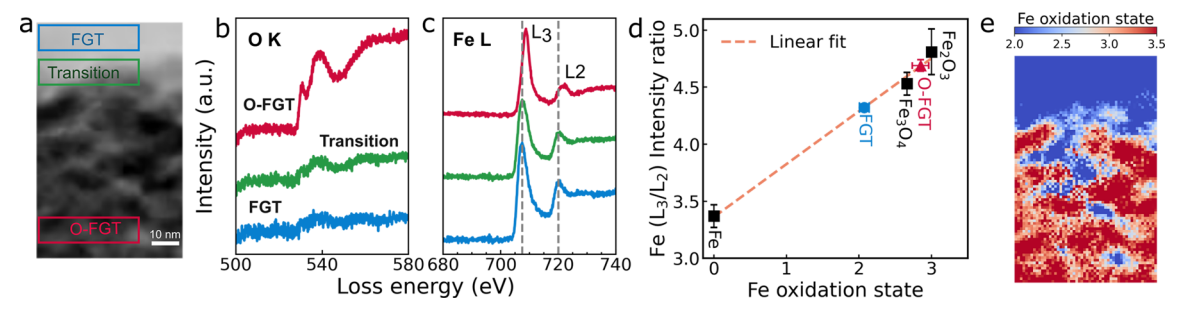


Figure 5. EELS analysis of Fe oxidation state in FGT. (a) STEM-ADF image across the FGT and O-FGT regions. ELNES spectra for background-subtracted (b) O-K and (c) Fe-L edges, averaged across the colored box regions in (a). In (c), the vertical dashed lines indicate the positions of the two Fe L-edge white lines for FGT. (d) Calibration curve showing the $Fe(L_3/L_2)$ white-line intensity ratio as a function of Fe oxidation state in Fe, Fe_2O_3 , and Fe_3O_4 reference samples, and in FGT and O-FGT. The orange dashed line is a linear fit to the data for the references (black squares). The estimated Fe oxidation states of FGT and O-FGT are 2.07 (\pm 0.07) and 2.85 (\pm 0.11), in which the uncertainties are calculated from four different regions of the sample. (e) Fe oxidation state map for region shown in (a).

may penetrate through edges and vacancy defects to react with sample.

The crystallinity of the film can strongly affect its magnetic properties. In order to further understand the effect of FGT oxidation on the crystallinity, we acquired high-resolution TEM (HRTEM) images and electron diffraction patterns from the various regions as shown in Figure 3d–f. The hexagonal pattern of FGT in the *ab* plane is seen in Figure 3d, as also shown schematically in Figure 4b. The selected area diffraction pattern (inset) confirms the hexagonal pattern. In the transition region (Figure 3e), we see a hexagonal pattern arising from pristine FGT mixed with deformed bright regions. Finally, in the O-FGT (Figure 3f), we see a mixed state comprising amorphous and polycrystalline regions with no evidence for the hexagonal pattern of the pristine FGT.

Determination of the variation of the composition in the ab plane of the FGT sample and imaging crystal structure of the plan-view FGT are also impacted due to the supporting bottom amorphous SiN_x membrane. Furthermore, since the magnetic domains we observed are Néel-type domains, which are stabilized by an interfacial DMI,^{32,33} it is important to analyze the structure and composition of the pure FGT and O-FGT along the c direction. We prepared a cross-section sample from a bulk FGT crystal, including the surface that had been exposed to air in order to observe similar effects of oxidation.

The cross-section HRTEM image (Figure 4a) shows the presence of two distinct regions, namely, the pristine FGT and the O-FGT. The pristine FGT (region I) shows clear lattice fringes as confirmed by the corresponding FFT. Figure 4c additionally shows an atomically resolved image of the crystal structure along the [120] zone axis. The positions of the Te, Fe, and Ge atoms are indicated by a schematic crystal structure. As described above, the O-FGT region shows a mixture of crystalline grains and amorphous regions (region II). The corresponding FFTs (Figure 4a, inset) support these observations. The crystalline regions are not oriented in any particular direction, supporting our earlier observation of the polycrystalline nature of O-FGT.

STEM-EDS measurements were further performed to understand the composition variation along the *c*-direction, as shown in Figure 4d. The pristine FGT shows uniform Fe, Ge, and Te elemental distributions as expected. However, the O-FGT region shows strong elemental clustering, seen as bright and dark regions in the HAADF-STEM image. These bright and dark regions correspond to the crystalline and amorphous regions in Figure 4a, respectively. Superimposing

the composition maps of Fe, Ge, and Te with the O map enables an understanding of the local compositional variation in the O-FGT region as shown in Figure 4e. There is a perfect overlap between the Fe (or Ge) and O maps, but the Te and O maps are anticorrelated. In Figure 4f, the average line profiles of Fe, Ge, Te, and O across the O-FGT and FGT regions also quantitatively show that clusters with higher oxygen content coincide with the rich Fe and Ge locations and do not coincide with the Te-rich locations. The Te-rich clusters (bright segment) are polycrystalline, whereas the Fe-Ge oxide clusters (dark segment) are amorphous (Supporting Information Figure S3). It is worthy to note that the Te-rich clusters still have lower-content oxygen in the O-FGT layer (Figure 4f). These findings demonstrate the preferential formation of Fe and Ge oxides. In order to gain insight into the oxidation state of the O-FGT, we performed EELS measurements.

3.3. Determination of Oxidation State. FGT has a sandwich crystal structure in each layer, consisting of $Te/Fe_1/Fe_2Ge/Fe_1/Te$ (Figure 4b), leading to the valence states of individual elements being: $(Fe_1^{3+})_2(Fe_2^{2+})(Ge^{4-})(Te^{2-})_2$. As discussed previously, in the O-FGT, the oxygen ions are found in the Fe–Ge-rich clusters. Fe has a higher electronegativity compared to Ge and Te and, therefore, would be expected to oxidize preferentially. Two types of Fe cation sites in FGT lead to the presence of both divalent (Fe_2^{+2}) and trivalent (Fe_1^{+3}) states. Therefore, we investigate the oxidation state of the Fe oxide using EELS, which provides high spatial and energy resolution. 35,36

We acquired spatially resolved EELS spectra across a region of the bulk FGT and the surface O-FGT in a cross-section sample, as shown in the annular dark-field (ADF) STEM image in Figure 5a. Parts b and c of Figure 5 show the energyloss near-edge structure (ELNES) peaks for the backgroundsubtracted O-K and Fe-L EELS edges. In Figure 5b, two significant O-K edge peaks are seen in the O-FGT, but only a small single peak is visible in the transition region. It should be noted that a small, weak O-K-edge ELNES peak is also seen in the pristine FGT, which is mostly due to the surface oxide formed on the TEM sample as it was exposed to air during loading and unloading. The Fe-L edge shows the typical L_3 and L_2 white-line peaks in all three regions (Figure 5c). The Fe Ledge peaks shift to a higher energy in the O-FGT as compared to the pristine FGT. The position of the white-line peaks is related to the oxidation state:³⁷ higher-energy peaks can be attributed to an increase in Fe valence state. 37,38 This is indicative of the oxidation process in the FGT, which has a

mixed Fe^{3+} and Fe^{2+} valence state, leading to an increase in the average Fe valence state in the oxide as compared to the pristine FGT.

The ratio of the integrated intensity of the Fe L_3 and L_2 white lines is also dependent on the oxidation state of the Fe. 27,37,38 The Fe (L_3/L_2) ratio was computed using the following steps: (1) removing the background signal from the EELS spectra using a step function; ^{27,35,37} (2) integrating the intensity underneath the Fe L_3 and L_2 peaks; and (3) evaluating the ratio of the integrated intensity of the Fe L_3/L_2 peaks. To determine the Fe valence state in the FGT and O-FGT from the white line ratio, we compared with the $Fe(L_3/L_3)$ L_2) intensity ratio from Fe reference materials, including pure Fe (Fe⁰), Fe₂O₃ (Fe³⁺), and Fe₃O₄ (mixed Fe²⁺and Fe³⁻ which we consider the average valence to be 2.67.³⁸⁻⁴⁰ This allows us to obtain a relationship between white-line ratio and Fe oxidation state, as plotted in Figure 5d. The $Fe(L_3/L_2)$ intensity ratio has a linear relationship with the Fe oxidation states determined from the reference materials (black squares). The average Fe oxidation state in FGT and O-FGT can thus be estimated by fitting a linear function to the data, giving values of approximately 2.07 (± 0.07) and 2.85 (± 0.11) for FGT and O-FGT, respectively. These values quantitatively indicate an increase in the valence state of Fe in O-FGT due to oxidation as compared to that in the pristine FGT. As the value of the white-line ratio in O-FGT is close to that of the Fe₂O₃ hematite phase, we expect that to be the dominant oxide formed in O-FGT. The estimated Fe valence state of the FGT is smaller than the theoretical value of +2.67 (2Fe³⁺ and 1Fe²⁺). The method we used merely allows for the rough calculation of valence state. The inelastic scattering events (such as sample thickness and crystal orientations) and EELS data processing (including background subtraction and fitting with the step function) contribute to the error of estimate of Fe oxidation state. Thus, here we only focus on how the relative change in the oxidation of Fe between FGT and O-FGT, rather than providing accurate values. The spatial variation of the white-line ratio can be used to map the Fe oxidation state as shown in Figure 5e in the region shown in Figure 5a. The Fe valence in the FGT is relatively uniform, with a nonuniform valence state in the O-FGT. The lower- and higher-valence regions correspond to Te-rich and Fe-rich clusters, respectively.

4. DISCUSSION AND CONCLUSIONS

We observed the presence of Néel-type magnetic domains in a pristine FGT flake with uniaxial anisotropy that was prepared under a vacuum and covered with graphite. Néel-type domains in perpendicular anisotropy materials typically occur due to an interfacial symmetry-breaking interaction, yet pristine FGT does not show such an interfacial asymmetry. The appearance of Bloch-type skyrmions has been reported in unoxidized FGT.²² However, we do not observe Bloch-type domain here. Another consideration is the magnetostatic energy, which is critical to determine the nature of magnetic domain wall, but the Bloch domain wall is energetically more favorable in particluar in a very thin films with the perpendicular anistropy as compared to Néel wall. 41 Recent theoretical work has shown that the fourth-order exchange interactions in monolayer FGT can result in an anisotropic interaction and yield a DMI-like effect to create mixed states consisting of either Bloch or Néel spin textures.⁴² These types of interaction can possibly explain our observations of Néel type skyrmions.

Furthermore, we observed an increase in the density of the domains and particularly of the Néel skyrmions under zeroapplied field when the sample was exposed to air. There are two possible mechanisms for boosting the formation of Néel skyrmions: exchange bias and surface roughness. Both these cases can be attributed to the presence of a surface oxidation layer. In the former case, the exchange bias can be created between an antiferromagnetic O-FGT phase and the ferromagnetic FGT. 12 Previous reports have shown that oxidized transition metal compounds can form an antiferromagnetic phase such as Co/CoO, 23 Fe/Fe₂O₃, 43 or oxidized Permalloy, 44 which leads to an exchange bias interaction when in contact with a ferromagnetic layer. We observed the formation of Fe-oxide in the O-FGT region, which showed a proportion of Fe^{3+} sites that is similar to Fe_2O_3 , which is antiferromagnetic. We therefore hypothesize that the O-FGT could be antiferromagnetic, which would also explain the disappearance of magnetic domains in the LTEM images of O-FGT. The interfacial exchange bias interaction between the ferromagnetic FGT and the antiferromagnetic surface oxide could support the formation of skyrmions in the absence of magnetic field. 46-48,48 Indeed, it has been reported that a directly oxidized layer or a polycrystalline antiferromagnetic layer can show a stronger exchange bias strength than a singlecrystal antiferromagnetic oxide. 49 Another possible factor contributing to the change in magnetic behavior is the significant roughness of the interface between O-FGT and FGT, seen in both the in-plane and cross-section TEM samples (Figures 3c and 4d). The rough interface morphology would have a strong effect on the exchange anisotropy, favoring the formation of circular magnetic domains akin to skyrmions in a ferromagnetic-antiferromagnetic system. 50,51

In summary, we have systematically examined how the degree of oxidation in nanoscale FGT influences the magnetic domain structure, chemical composition, and crystallinity. The promotion of Néel skyrmion formation was observed when the FGT was exposed to air under zero-field conditions. The O-FGT forms an Fe-based oxide in Fe-Ge-rich clusters, and the crystallinity changes from a single crystal lattice to a mixture of polycrystalline and amorphous regions. EELS result reveals that the average Fe oxidation state is closer to Fe³⁺ in O-FGT, possibly leading to O-FGT being antiferromagnetic. This then leads to the introduction of a unidirectional anistropy, namely, exchange bias, between the ferromagnetic FGT and antiferromagnetic O-FGT, resulting in creation of a denser skyrmion array. Our results also show that the nonuniform O-FGT leads to a rough interface between O-FGT and FGT, which could also possibly give rise to the preferential creation of bubble-shape domains. Thus, this work demonstrates that a controlled degree of surface oxidation in FGT films is beneficial to supporting the creation of skyrmions under zero-field conditions for future applications in spintronic devices.

ASSOCIATED CONTENT

Supporting Information

The Supporting Information is available free of charge at https://pubs.acs.org/doi/10.1021/acsanm.2c05479.

Details of FGT TEM samples, raw LTEM images of the FGT before and after oxidizing, and average EDS spectra (PDF)

AUTHOR INFORMATION

Corresponding Author

Charudatta Phatak — Materials Science Division, Argonne National Laboratory, Lemont, Illinois 60439, United States; Department of Materials Science and Engineering, Northwestern University, Evanston, Illinois 60208, United States; orcid.org/0000-0002-8931-0296; Email: cd@anl.gov

Authors

- Yue Li Materials Science Division, Argonne National Laboratory, Lemont, Illinois 60439, United States;
 o orcid.org/0000-0001-9171-0355
- Xiaobing Hu Department of Materials Science and Engineering, Northwestern University, Evanston, Illinois 60208, United States; oorcid.org/0000-0002-9233-8118
- Arash Fereidouni Department of Physics, University of Arkansas, Fayetteville, Arkansas 72701, United States
- Rabindra Basnet Department of Physics, University of Arkansas, Fayetteville, Arkansas 72701, United States
- Krishna Pandey Materials Science and Engineering Program, University of Arkansas, Fayetteville, Arkansas 72701, United States
- Jianguo Wen Center for Nanoscale Materials, Argonne National Laboratory, Lemont, Illinois 60439, United States; orcid.org/0000-0002-3755-0044
- Yuzi Liu Center for Nanoscale Materials, Argonne National Laboratory, Lemont, Illinois 60439, United States;
 orcid.org/0000-0002-8733-1683
- Hong Zheng Materials Science Division, Argonne National Laboratory, Lemont, Illinois 60439, United States
- Hugh O. H. Churchill Department of Physics, University of Arkansas, Fayetteville, Arkansas 72701, United States; Materials Science and Engineering Program, University of Arkansas, Fayetteville, Arkansas 72701, United States
- Jin Hu Department of Physics, University of Arkansas, Fayetteville, Arkansas 72701, United States; Materials Science and Engineering Program, University of Arkansas, Fayetteville, Arkansas 72701, United States; orcid.org/0000-0003-0080-4239
- Amanda K. Petford-Long Materials Science Division, Argonne National Laboratory, Lemont, Illinois 60439, United States; Department of Materials Science and Engineering, Northwestern University, Evanston, Illinois 60208, United States

Complete contact information is available at: https://pubs.acs.org/10.1021/acsanm.2c05479

Notes

The authors declare no competing financial interest.

ACKNOWLEDGMENTS

This work was funded by the US Department of Energy, Office of Science, Office of Basic Energy Sciences, Materials Science and Engineering Division. Work performed at the Center for Nanoscale Materials, a U.S. Department of Energy Office of Science User Facility, was supported by the U.S. DOE, Office of Basic Energy Sciences, under Contract No. DE-AC02-06CH11357. Single crystal growth was supported by the U.S. Department of Energy, Office of Science, Basic Energy Sciences program under Grant No. DE-SC0022006. This work made use of the EPIC facility of Northwestern

University's NUANCE Center, which has received support from the SHyNE Resource (NSF ECCS-2025633), the IIN, and Northwestern's MRSEC program (NSF DMR-1720139). H.O.H.C. acknowledges support from NSF award DMR-1848281, and the authors acknowledge the MonArk NSF Quantum Foundry supported by the National Science Foundation Q-AMASE-i program under NSF award No. DMR-1906383.

REFERENCES

- (1) Burch, K. S.; Mandrus, D.; Park, J.-G. Magnetism in two-dimensional van der Waals materials. *Nature* **2018**, *563*, 47–52.
- (2) Fei, Z.; Huang, B.; Malinowski, P.; Wang, W.; Song, T.; Sanchez, J.; Yao, W.; Xiao, D.; Zhu, X.; May, A. F.; Wu, W.; Cobden, D. H.; Chu, J.-H.; Xu, X. Two-dimensional itinerant ferromagnetism in atomically thin Fe₃GeTe₂. *Nat. Mater.* **2018**, *17*, 778–782.
- (3) Wu, Y.; Zhang, S.; Zhang, J.; Wang, W.; Zhu, Y. L.; Hu, J.; Yin, G.; Wong, K.; Fang, C.; Wan, C.; Han, X.; Shao, Q.; Taniguchi, T.; Watanabe, K.; Zang, J.; Mao, Z.; Zhang, X.; Wang, K. L. Néel-type skyrmion in WTe₂/Fe₃GeTe₂ van der Waals heterostructure. *Nat. Commun.* **2020**, *11*, 3860.
- (4) Peng, L.; Yasin, F. S.; Park, T.-E.; Kim, S. J.; Zhang, X.; Nagai, T.; Kimoto, K.; Woo, S.; Yu, X. Tunable Néel–Bloch Magnetic Twists in Fe₃GeTe₂ with van der Waals Structure. *Adv. Funct. Mater.* **2021**, *31*, 2103583.
- (5) Gao, Y.; Yin, Q.; Wang, Q.; Li, Z.; Cai, J.; Zhao, T.; Lei, H.; Wang, S.; Zhang, Y.; Shen, B. Spontaneous (Anti)Meron chains in the domain walls of van der Waals ferromagnetic Fe_{5-x}GeTe₂. *Adv. Mater.* **2020**, 32, 2005228.
- (6) Han, M.-G.; Garlow, J. A.; Liu, Y.; Zhang, H.; Li, J.; DiMarzio, D.; Knight, M. W.; Petrovic, C.; Jariwala, D.; Zhu, Y. Topological magnetic-spin textures in two-dimensional van der Waals Cr₂Ge₂Te₆. *Nano Lett.* **2019**, *19*, 7859–7865.
- (7) Deng, Y.; Yu, Y.; Song, Y.; Zhang, J.; Wang, N. Z.; Sun, Z.; Yi, Y.; Wu, Y. Z.; Wu, S.; Zhu, J.; Wang, J.; Chen, X. H.; Zhang, Y. Gatetunable room-temperature ferromagnetism in two-dimensional Fe₃GeTe₂. *Nature* **2018**, *563*, 94–99.
- (8) Yang, M.; Li, Q.; Chopdekar, R. V.; Stan, C.; Cabrini, S.; Choi, J. W.; Wang, S.; Wang, T.; Gao, N.; Scholl, A.; Tamura, N.; Hwang, C.; Wang, F.; Qiu, Z. Highly Enhanced Curie Temperature in Ga-Implanted Fe₃GeTe₂ van der Waals Material. *Adv. Quantum Technol.* **2020**, *3*, 2000017.
- (9) Wang, Y.; Wang, C.; Liang, S.-J.; Ma, Z.; Xu, K.; Liu, X.; Zhang, L.; Admasu, A. S.; Cheong, S.-W.; Wang, L.; Chen, M.; Liu, Z.; Cheng, B.; Ji, W.; Miao, F. Strain-sensitive magnetization reversal of a van der Waals magnet. *Adv. Mater.* **2020**, *32*, 2004533.
- (10) Novoselov, K. S.; Mishchenko, A.; Carvalho, A.; Castro Neto, A. H. 2D materials and van der Waals heterostructures. *Science* **2016**, 353, aac9439.
- (11) Geim, A. K.; Grigorieva, I. V. Van der Waals heterostructures. *Nature* **2013**, 499, 419–425.
- (12) Gweon, H. K.; Lee, S. Y.; Kwon, H. Y.; Jeong, J.; Chang, H. J.; Kim, K.-W.; Qiu, Z. Q.; Ryu, H.; Jang, C.; Choi, J. W. Exchange bias in weakly interlayer-coupled van der Waals magnet Fe₃GeTe₂. *Nano Lett.* **2021**, *21*, 1672–1678.
- (13) Srivastava, P. K.; Hassan, Y.; Ahn, H.; Kang, B.; Jung, S.-G.; Gebredingle, Y.; Joe, M.; Abbas, M. S.; Park, T.; Park, J.-G.; Lee, K.-J.; Lee, C. Exchange bias effect in ferro-/antiferromagnetic van der Waals heterostructures. *Nano Lett.* **2020**, *20*, *3978*–*3985*.
- (14) Choi, E.-M.; Sim, K. I.; Burch, K. S.; Lee, Y. H. Emergent Multifunctional Magnetic Proximity in van der Waals Layered Heterostructures. *Adv. Sci.* **2022**, *9*, 2200186.
- (15) Sierra, J. F.; Fabian, J.; Kawakami, R. K.; Roche, S.; Valenzuela, S. O. Van der Waals heterostructures for spintronics and optospintronics. *Nat. Nanotechnol.* **2021**, *16*, 856–868.
- (16) Li, H.; Ruan, S.; Zeng, Y.-J. Intrinsic van der Waals magnetic materials from bulk to the 2D limit: new frontiers of spintronics. *Adv. Mater.* **2019**, *31*, 1900065.

- (17) Ciarrocchi, A.; Tagarelli, F.; Avsar, A.; Kis, A. Excitonic devices with van der Waals heterostructures: valleytronics meets twistronics. *Nat. Rev. Mater.* **2022**, *7*, 449–464.
- (18) Du, L.; Tang, J.; Zhao, Y.; Li, X.; Yang, R.; Hu, X.; Bai, X.; Wang, X.; Watanabe, K.; Taniguchi, T.; Shi, D.; Yu, G.; Bai, X.; Hasan, T.; Zhang, G.; Sun, Z. Lattice Dynamics, Phonon Chirality, and Spin—Phonon Coupling in 2D Itinerant Ferromagnet Fe₃GeTe₂. *Adv. Funct. Mater.* **2019**, 29, 1904734.
- (19) Zhu, R.; Zhang, W.; Shen, W.; Wong, P. K. J.; Wang, Q.; Liang, Q.; Tian, Z.; Zhai, Y.; Qiu, C.-w.; Wee, A. T. S. Exchange bias in van der Waals CrCl₃/Fe₃GeTe₂ heterostructures. *Nano Lett.* **2020**, 20, 5030–5035.
- (20) Hu, G.; Zhu, Y.; Xiang, J.; Yang, T.-Y.; Huang, M.; Wang, Z.; Wang, Z.; Liu, P.; Zhang, Y.; Feng, C.; Hou, D.; Zhu, W.; Gu, M.; Hsu, C.-H.; Chuang, F.-C.; Lu, Y.; Xiang, B.; Chueh, Y. Antisymmetric magnetoresistance in a van der Waals antiferromagnetic/ferromagnetic layered MnPS₃/Fe₃GeTe₂ stacking heterostructure. *ACS Nano* **2020**, *14*, 12037–12044.
- (21) Kim, D.; Park, S.; Lee, J.; Yoon, J.; Joo, S.; Kim, T.; Min, K.-j.; Park, S.-Y.; Kim, C.; Moon, K.-W.; Lee, C.; Hong, J.; Hwang, C. Antiferromagnetic coupling of van der Waals ferromagnetic Fe₃GeTe₂. *Nanotechnology* **2019**, *30*, 245701.
- (22) Park, T.-E.; Peng, L.; Liang, J.; Hallal, A.; Yasin, F. S.; Zhang, X.; Song, K. M.; Kim, S. J.; Kim, K.; Weigand, M.; Schütz, G.; Finizio, S.; Raabe, J.; Garcia, K.; Xia, J.; Zhou, Y.; Ezawa, M.; Liu, X.; Chang, J.; Koo, H. C.; et al. Néel-type skyrmions and their current-induced motion in van der Waals ferromagnet-based heterostructures. *Phys. Rev. B* **2021**, *103*, 104410.
- (23) Gierlings, M.; Prandolini, M. J.; Fritzsche, H.; Gruyters, M.; Riegel, D. Change and asymmetry of magnetization reversal for a Co/CoO exchange-bias system. *Phys. Rev. B* **2002**, *65*, 092407.
- (24) Zysler, R.; Fiorani, D.; Ďormann, J. L.; Testa, A. M. Magnetic properties of ultrafine α -Fe₂O₃ antiferromagnetic particles. *J. Magn. Magn. Mater.* **1994**, 133, 71–73.
- (25) Thompson, J. P.; Doha, M. H.; Murphy, P.; Hu, J.; Churchill, H. O. H. Exfoliation and analysis of large-area, air-sensitive two-dimensional materials. *JoVE* (*Journal of Visualized Experiments*) **2019**, 143, No. e58693.
- (26) Xie, L.; Du, L.; Lu, X.; Yang, R.; Shi, D.; Zhang, G. A facile and efficient dry transfer technique for two-dimensional Van der Waals heterostructure. *Chin. Phys. B* **2017**, *26*, 087306.
- (27) Pearson, D. H.; Ahn, C. C.; Fultz, B. White lines and *d*-electron occupancies for the 3*d* and 4*d* transition metals. *Phys. Rev. B* **1993**, 47, 8471.
- (28) Jiang, W.; Zhang, S.; Wang, X.; Phatak, C.; Wang, Q.; Zhang, W.; Jungfleisch, M. B.; Pearson, J. E.; Liu, Y.; Zang, J.; Cheng, X.; Petford-Long, A.; Hoffmann, A.; te Velthuis, S. G. E. Quantifying chiral exchange interaction for Néel-type skyrmions via Lorentz transmission electron microscopy. *Phys. Rev. B* **2019**, *99*, 104402.
- (29) McCray, A. R.; Cote, T.; Li, Y.; Petford-Long, A. K.; Phatak, C. Understanding Complex Magnetic Spin Textures with Simulation-Assisted Lorentz Transmission Electron Microscopy. *Phys. Rev. Applied* **2021**, *15*, 044025.
- (30) Zhang, T.; Zhang, Y.; Huang, M.; Li, B.; Sun, Y.; Qu, Z.; Duan, X.; Jiang, C.; Yang, S. Tuning the Exchange Bias Effect in 2D van der Waals Ferro-/Antiferromagnetic Fe₃GeTe₂/CrOCl Heterostructures. *Adv. Sci.* **2022**, *9*, 2105483.
- (31) Li, Y.; Basnet, R.; Pandey, K.; Hu, J.; Wang, W.; Ma, X.; McCray, A. R.; Petford-Long, A. K.; Phatak, C. Field-Dependent Magnetic Domain Behavior in van der Waals Fe₃GeTe₂. *JOM* **2022**, 74, 2310–2318.
- (32) Fert, A.; Reyren, N.; Cros, V. Magnetic skyrmions: advances in physics and potential applications. *Nat. Rev. Mater.* **2017**, *2*, 17031.
- (33) Pollard, S. D.; Garlow, J. A.; Yu, J.; Wang, Z.; Zhu, Y.; Yang, H. Observation of stable Néel skyrmions in cobalt/palladium multilayers with Lorentz transmission electron microscopy. *Nat. Commun.* **2017**, *8*, 14761.
- (34) Deiseroth, H.-J.; Aleksandrov, K.; Reiner, C.; Kienle, L.; Kremer, R. K. Fe₃GeTe₂ and Ni₃GeTe₂-Two New Layered

- Transition-Metal Compounds: Crystal Structures, HRTEM Investigations, and Magnetic and Electrical Properties. *Eur. J. Inorg. Chem.* **2006**, 2006, 1561–1567.
- (35) Hu, X.; Huang, J.; Wu, L.; Kaltak, M.; Fernandez-Serra, M. V.; Meng, Q.; Wang, L.; Marschilok, A. C.; Takeuchi, E. S.; Takeuchi, K. J.; Hybertsen, M. S.; Zhu, Y. Atomic scale account of the surface effect on ionic transport in silver hollandite. *Chem. Mater.* **2018**, *30*, 6124–6133.
- (36) Suenaga, K.; Koshino, M. Atom-by-atom spectroscopy at graphene edge. *Nature* **2010**, *468*, 1088–1090.
- (37) Tan, H.; Verbeeck, J.; Abakumov, A.; Van Tendeloo, G. Oxidation state and chemical shift investigation in transition metal oxides by EELS. *Ultramicroscopy* **2012**, *116*, 24–33.
- (38) Schmid, H. K.; Mader, W. Oxidation states of Mn and Fe in various compound oxide systems. *Micron* **2006**, *37*, 426–432.
- (39) Brollo, M. E. F.; López-Ruiz, R.; Muraca, D.; Figueroa, S. J.; Pirota, K. R.; Knobel, M. Compact Ag@Fe₃O₄ core-shell nanoparticles by means of single-step thermal decomposition reaction. *Sci. Rep.* **2014**, *4*, 6839.
- (40) Schmuki, P.; Virtanen, S.; Davenport, A. J.; Vitus, C. M. In situ X-Ray absorption near-edge spectroscopic study of the cathodic reduction of artificial Iron oxide passive films. *J. Electrochem. Soc.* **1996**, *143*, 574.
- (41) Hubert, A.; Schäfer, R. Magnetic domains: the analysis of magnetic microstructures; Springer Science & Business Media, 2008; pp 263–264.
- (42) Xu, C.; Li, X.; Chen, P.; Zhang, Y.; Xiang, H.; Bellaiche, L. Assembling diverse skyrmionic phases in Fe_3GeTe_2 monolayers. Adv. *Mater.* **2022**, 34, 2107779.
- (43) Guo, J.; Zhao, X.; Lu, Z.; Shi, P.; Tian, Y.; Chen, Y.; Yan, S.; Bai, L.; Harder, M. High exchange-bias blocking temperature in an ultrathin amorphous antiferromagnet system. *Phys. Rev. B* **2021**, *104*, L100401.
- (44) Hagedorn, F. B. Exchange anisotropy in oxidized permalloy thin films at low temperatures. *J. Appl. Phys.* **1967**, *38*, 3641–3645.
- (45) Morrish, A. H. Canted antiferromagnetism: hematite; World Scientific, 1994; pp 1-2.
- (46) Guang, Y.; Bykova, I.; Liu, Y.; Yu, G.; Goering, E.; Weigand, M.; Gräfe, J.; Kim, S. K.; Zhang, J.; Zhang, H.; Yan, Z.; Wan, C.; Feng, J.; Wang, X.; Guo, C.; Wei, H.; Peng, Y.; Tserkovnyak, Y.; Han, X.; Schütz, G. Creating zero-field skyrmions in exchange-biased multilayers through X-ray illumination. *Nat. Commun.* **2020**, *11*, 949.
- (47) Rana, K. G.; Finco, A.; Fabre, F.; Chouaieb, S.; Haykal, A.; Buda-Prejbeanu, L.; Fruchart, O.; Le Denmat, S.; David, P.; Belmeguenai, M.; Denneulin, T.; Dunin-Borkowski, R. E.; Gaudin, G.; Jacques, V.; Boulle, O. Room-temperature skyrmions at zero field in exchange-biased ultrathin films. *Phys. Rev. Applied* **2020**, *13*, 044079.
- (48) Guang, Y.; Peng, Y.; Yan, Z.; Liu, Y.; Zhang, J.; Zeng, X.; Zhang, S.; Zhang, S.; Burn, D. M.; Jaouen, N.; Wei, J.; Xu, H.; Feng, J.; Fang, C.; Laan, G.; Hesjedal, T.; Cui, B.; Zhang, X.; Yu, G.; Han, X. Electron beam lithography of magnetic skyrmions. *Adv. Mater.* **2020**, 32, 2003003.
- (49) Nogués, J.; Schuller, I. K. Exchange bias. J. Magn. Magn. Mater. 1999, 192, 203–232.
- (50) Malozemoff, A. P. Heisenberg-to-Ising crossover in a random-field model with uniaxial anisotropy. *Phys. Rev. B* **1988**, *37*, 7673.
- (51) Malozemoff, A. P. Random-field model of exchange anisotropy at rough ferromagnetic-antiferromagnetic interfaces. *Phys. Rev. B* **1987**, 35, 3679.